Available online at www.sciencedirect.com
SCIENCE DIRECT®
Acta Materialia 53 (2005) 2845–2855
Acta MATERIALIA
www.actamat-journals.com

Phase-field microelasticity theory and micromagnetic simulations of domain structures in giant magnetostrictive materials

J.X. Zhang *, L.Q. Chen

Department of Materials Science and Engineering, The Pennsylvania State University, 305 Steidle Building, University Park, State College, PA 16802, United States

Received 17 December 2004; received in revised form 27 February 2005; accepted 2 March 2005
Available online 7 April 2005

Abstract

A computational model is proposed to predict the stability of magnetic domain structures and their temporal evolution in giant magnetostrictive materials by combining a micromagnetic model with the phase-field microelasticity theory of Khachaturyan. The model includes all the important energetic contributions, including the magnetocrystalline anisotropy energy, exchange energy, magnetostatic energy, external field energy, and elastic energy. While the elastic energy of an arbitrary magnetic domain structure is obtained analytically in Fourier space, the Landau–Liftshitz–Gilbert equation is solved using the efficient Gauss–Seidel projection method. Both $Fe_{81.3}Ga_{18.7}$ and Terfenol-D are considered as examples. The effects of elastic energy and magnetostatic energy on domain structures are studied. The magnetostriction and associated domain structure evolution under an applied field are modeled under different pre-stress conditions. It is shown that a compressive pre-stress can efficiently increase the overall magnetostrictive effect. The results are compared with existing experiment measurements and observations.

Keywords: Phase-field models; Simulation; Domain structure; Magnetostriction

1. Introduction

Magnetostriction is a phenomenon in which a material changes its physical dimensions when there is a change in its magnetization. The change in magnetization can be induced by the application of a magnetic field or a stress field. Magnetostriction is observed, to differing degrees, in all ferromagnetic materials. While typical magnetostrictive strains of magnetic materials are of the order of 10^{-5}–10^{-6}, some compounds containing rare earth elements have magnetostriction as high as 10^{-3}. Among these, Terfenol-D ($Tb_xDy_{1-x}Fe_2$, $x = 0.3$) has been extensively investigated for use in sensor and actuator devices because of its high magnetostriction to anisotropy ratio [1,2]. It has been recently found that large magnetostriction (over 200 ppm) at room temperature also occurs in FeGa alloys with disordered body-centered cubic α-Fe structure [3–5].

Giant magnetostrictive materials often display complex domain structures that arise from the competition of the magnetocrystalline anisotropy energy, exchange energy, magnetostatic energy, external field energy, and elastic energy. The domain evolution under applied fields is directly responsible for the overall strain response of the materials. Therefore, the domain structures and their evolution have been extensively studied experimentally [6–15]. To explain the observed magnetic behavior, there have also been a number of theoretical developments for magnetostrictive materials, including the works by Brown [16], James and Kinderlehrer [17,18], and DeSimone and James [19]. However, due to the rather complicated elastic solutions associated with an arbitrary domain structure, there has been

* Corresponding author. Tel.: +1 814 865 0389; fax: +1 814 865 2917.
E-mail address: jzz108@psu.edu (J.X. Zhang).

1359-6454/$30.00
doi:10.1016/j.actamat.2005.03.002

essentially no simulation of macroscopically inhomogeneous domain patterns and their evolution under external fields in giant magnetostrictive materials.

One type of approach assumed that the magnetizations of domains are constrained by the anisotropy energy to lie along the easy magnetic axes. The ferromagnetic constitutive behavior was then described by the distribution of a fixed quantity of available magnetic domains within materials among all the possible directions. The model assumed that each domain is magnetized independently without being affected by the magnetization states of neighboring domains. This type of approach has been used in many works to study the magnetostriction under an external magnetic field [20–24]. But this model is not suitable for describing a material with low magnetocrystalline anisotropy or the system states close to saturation when the magnetic field is applied along directions far away from those of easy axes. Zhu et al. [25] studied the influence of external stress on the cohesive field in magnetic thin films. In their micromagnetic model, without solving the total compatible strain, they use the stress-free magnetostrictive strain caused by the magnetization instead; thus the intrinsic stress resulting from the elastic incompatibility of magnetostrictive strains is not taken into account. The intrinsic stress is critically important for materials with large magnetostriction [26]. Fabian and Heider [27] have calculated the magnetostrictive self-energies of a magnetic particle imbedded in a non-magnetic matrix using the finite element method and the continuum theory of defects. Recently, Shu et al. [26,28] developed a modified boundary integral formalism to calculate the intrinsic stress induced by incompatible magnetostrictive strains, but their method is confined to some simple two-dimensional (2D) cases due to the complexity of solving the elastic equilibrium equations.

The main purpose of this paper is to describe a computational approach to model the stability and evolution of magnetic domain structures in giant magnetostrictive materials. It combines the micromagnetic model for magnetic domain evolution [29] and the phase-field microelasticity theory [30,31] for the elastic solutions in a magnetostrictive material with arbitrary distributions of magnetic domains. The phase-field microelasticity theory has been extensively used in computer simulations of structural phase transformations and microstructure evolution in both bulk systems, see, for example, Refs. [32–34], and for more extensive references [35], and thin films [36–38]. The model is able to predict the detailed domain structure and their evolution under an applied field without a priori assumptions on domain morphologies. The main limitation of the present model as well as essentially all prior phase-field models for solid state phase transformations is the assumption of periodic boundary conditions, and hence the results are only valid when the simulation system size is much smaller than the actual sample size. It will be shown that the domain shapes and domain wall configuration in magnetostrictive materials predicted from the model automatically satisfy the condition of magnetic and elastic compatibilities. The domain structure and magnetostriction evolution under a magnetic field will also be studied for samples with different magnitudes of applied pre-stress. The results predicted from our simulations will be compared with existing experimental observation and theoretical predictions.

2. Micromagnetic model and phase-field elasticity theory

In a micromagnetic model, the domain structure is described by the spatial distribution of the local magnetization $\mathbf{M}(\mathbf{r})$. The temporal evolution of the magnetization configuration, thus the domain structure, is described by the Landau–Lifshitz–Gilbert (LLG) equation

$$(1+\alpha^2)\frac{\partial \mathbf{M}}{\partial t} = -\gamma_0 \mathbf{M}\times\mathbf{H}_{\text{eff}} - \frac{\gamma_0\alpha}{M_s}\mathbf{M}\times(\mathbf{M}\times\mathbf{H}_{\text{eff}}), \quad (1)$$

where M_s is the saturation magnetization, γ_0 is the gyromagnetic ratio, α is the damping constant, and $\mathbf{H}_{\text{eff}}$ is the effective magnetic field, which can be represented as a variational derivative of the total free energy of the system with respect to magnetization

$$\mathbf{H}_{\text{eff}} = -\frac{1}{\mu_0}\frac{\partial E}{\partial \mathbf{M}}, \quad (2)$$

where μ_0 is the permeability of vacuum, the total free energy of magnetostricitve materials is given by

$$E = E_{\text{anis}} + E_{\text{exch}} + E_{\text{ms}} + E_{\text{external}} + E_{\text{elastic}}, \quad (3)$$

where E_{anis}, E_{exch}, E_{ms}, E_{external}, E_{elastic} are the magnetocrystalline anisotropy energy, exchange energy, magnetostatic energy, external field energy, and elastic energy, respectively.

The magnetocrystalline anisotropy energy of a cubic crystal is

$$E_{\text{anis}} = \int \left[K_1(m_1^2m_2^2 + m_1^2m_3^2 + m_2^2m_3^2) + K_2 m_1^2m_2^2m_3^2\right] \mathrm{d}V, \quad (4)$$

where m_i are the components of the unit magnetization vector, $\mathbf{m} = \mathbf{M}/M_s$. K_1 and K_2 are the anisotropy constants.

The exchange energy is determined solely by the spatial variation of the magnetization orientation and can be written as

$$E_{\text{exch}} = A\int (m_{1,1}^2 + m_{1,2}^2 + m_{1,3}^2 + m_{2,1}^2 + m_{2,2}^2 + m_{2,3}^2 + m_{3,1}^2 + m_{3,2}^2 + m_{3,3}^2)\,\mathrm{d}V, \quad (5)$$

where A is the exchange stiffness constant. In this paper, a comma in a subscript stands for spatial differentiation,

for example, $m_{i,j} = \partial m_i/\partial x_j$, where x_j is the jth component of position vector in the Cartesian coordinates.

The magnetostatic energy of a system can be written as

$$E_{\mathrm{ms}} = -\frac{1}{2}\mu_0 M_{\mathrm{s}} \int \mathbf{H}_{\mathrm{d}} \cdot \mathbf{m}\, \mathrm{d}V, \tag{6}$$

where $\mathbf{H}_{\mathrm{d}}$ is the stray field that is determined by the long-range interaction among the magnetic moments in the system. The stray field $\mathbf{H}_{\mathrm{d}}$ is governed by [29]

$$H_{\mathrm{d}1,1} + H_{\mathrm{d}2,2} + H_{\mathrm{d}3,3} = -M_{\mathrm{s}}(m_{1,1} + m_{2,2} + m_{3,3}), \tag{7}$$

where $H_{\mathrm{d}i}$ are the components of $\mathbf{H}_{\mathrm{d}}$. By introducing magnetic scalar potential ϕ,

$$H_{\mathrm{d}i} = -\phi_{,i}. \tag{8}$$

Eq. (7) is thus rewritten as,

$$\Delta\phi = M_{\mathrm{s}}(m_{1,1} + m_{2,2} + m_{3,3}). \tag{9}$$

The solution of the potential for Eq. (9) is given in Fourier space by,

$$\phi(\xi) = -i\frac{M_{\mathrm{s}}[m_1(\xi)\xi_1 + m_2(\xi)\xi_2 + m_3(\xi)\xi_3]}{\xi_1^2 + \xi_2^2 + \xi_3^2}, \tag{10}$$

where $i = \sqrt{-1}$, ξ_i are the coordinates in Fourier space, and $\phi(\xi)$, $m_i(\xi)$ are the Fourier transforms of ϕ and m_i, respectively. The value of ϕ in real space can be obtained through an inverse Fourier transform of $\phi(\xi)$. The value of $\mathbf{H}_{\mathrm{d}}$ can then be calculated by Eq. (8).

Note that the origin of the Fourier space ($\xi_1 = \xi_2 = \xi_3 = 0$) is a singularity point in Eq. (10) and its contribution corresponds to the demagnetization field caused by the average magnetization of the system. This can easily be seen by writing the local magnetization field as

$$\mathbf{M}(\mathbf{r}) = \bar{\mathbf{M}} + \delta\mathbf{M}(\mathbf{r}), \tag{11}$$

where $\bar{\mathbf{M}}$ is spatially independent average magnetization and $\delta\mathbf{M}$ is the spatially dependent heterogeneous part of the magnetization field. The average field $\bar{\mathbf{M}}$ is defined in such a way that $\int \delta\mathbf{M}(\mathbf{r})\, \mathrm{d}V = 0$. Since the contribution from ($\xi_1 = \xi_2 = \xi_3 = 0$) is excluded in Eq. (10), it only includes the contribution from the heterogeneous part of the magnetization field $\delta\mathbf{M}$. Therefore, in order to consider the demagnetization field caused by the average magnetization in this work, we approximate the demagnetization field by

$$\mathbf{H}_{\mathrm{d}}(\bar{\mathbf{M}}) = N\bar{\mathbf{M}}, \tag{12}$$

where N is the demagnetizing factor, which depends only on the shape of the specimen. It should be pointed out since we assume periodic boundary conditions for the heterogeneous magnetization, Eq. (12) is an approximation for incorporating the effect of sample shape on domain structures. Such an approximation is, in principle, only valid if the simulation system size is much smaller than the real sample size to be simulated. Although the demagnetization factor, N, is known for certain specific shapes, in general, it has to be computed numerically.

The effect of an external applied magnetic field $\mathbf{H}_{\mathrm{ex}}$ on the system energy can be taken into account through the interaction between the magnetization and the external field

$$E_{\mathrm{external}} = -\mu_0 M_{\mathrm{s}} \int \mathbf{H}_{\mathrm{ex}} \cdot \mathbf{m}\, \mathrm{d}V. \tag{13}$$

For a cubic magnetostrictive material, the deformation associated with the local magnetization is described by the stress-free strain:

$$\begin{aligned}
\varepsilon_{11}^0 &= \frac{3}{2}\lambda_{100}\left(m_1^2 - \frac{1}{3}\right), \quad \varepsilon_{12}^0 = \frac{3}{2}\lambda_{111} m_1 m_2, \\
\varepsilon_{22}^0 &= \frac{3}{2}\lambda_{100}\left(m_2^2 - \frac{1}{3}\right), \quad \varepsilon_{13}^0 = \frac{3}{2}\lambda_{111} m_1 m_3, \\
\varepsilon_{33}^0 &= \frac{3}{2}\lambda_{100}\left(m_3^2 - \frac{1}{3}\right), \quad \varepsilon_{23}^0 = \frac{3}{2}\lambda_{111} m_2 m_3,
\end{aligned} \tag{14}$$

where λ_{100} and λ_{111} are the magnetostrictive constants of a cubic crystal.

To accommodate the local deformations arising from the magnetostrictive effect, the elastic strains e_{ij} and thus elastic energy E_{elastic} are generated in a magnetic domain structure,

$$e_{ij} = \varepsilon_{ij} - \varepsilon_{ij}^0, \tag{15}$$

where ε_{ij} is the total strain. The corresponding elastic energy can be expressed as

$$E_{\mathrm{elastic}} = \int \frac{1}{2} c_{ijkl} e_{ij} e_{kl}\, \mathrm{d}V = \int \frac{1}{2} c_{ijkl}(\varepsilon_{ij} - \varepsilon_{ij}^0)(\varepsilon_{kl} - \varepsilon_{kl}^0)\, \mathrm{d}V, \tag{16}$$

where c_{ijkl} is the elastic stiffness tensor. The summation convention for the repeated indices is employed and i, j, k, $l = 1, 2, 3$. For a cubic material with its three independent elastic constant c_{11}, c_{12} and c_{44} in the Voigt's notation, the elastic energy can be rewritten as

$$\begin{aligned}
E_{\mathrm{elastic}} = \int \Big\{ & \frac{1}{2} c_{11}(e_{11}^2 + e_{22}^2 + e_{33}^2) \\
& + c_{12}(e_{11}e_{22} + e_{22}e_{33} + e_{11}e_{33}) \\
& + 2c_{44}(e_{12}^2 + e_{23}^2 + e_{13}^2) \Big\}\, \mathrm{d}V \\
= \int \Big\{ & \frac{1}{2} c_{11}[(\varepsilon_{11} - \varepsilon_{11}^0)^2 + (\varepsilon_{22} - \varepsilon_{22}^0)^2 + (\varepsilon_{33} - \varepsilon_{33}^0)^2] \\
& + c_{12}[(\varepsilon_{11} - \varepsilon_{11}^0)(\varepsilon_{22} - \varepsilon_{22}^0) + (\varepsilon_{22} - \varepsilon_{22}^0)(\varepsilon_{33} - \varepsilon_{33}^0) \\
& + (\varepsilon_{11} - \varepsilon_{11}^0)(\varepsilon_{33} - \varepsilon_{33}^0)] + 2c_{44}[(\varepsilon_{12} - \varepsilon_{12}^0)^2 \\
& + (\varepsilon_{23} - \varepsilon_{23}^0)^2 + (\varepsilon_{13} - \varepsilon_{13}^0)^2] \Big\}\, \mathrm{d}V
\end{aligned} \tag{17}$$

which can be separated into three contributions,

$$E_{\text{elastic}} = E_{\text{elastic1}} + E_{\text{elastic2}} + E_{\text{elastic3}} \tag{18}$$

with

$$\begin{aligned} E_{\text{elastic1}} = \int \Big\{ & \frac{1}{2} c_{11}(\varepsilon_{11}^2 + \varepsilon_{22}^2 + \varepsilon_{33}^2) \\ & + c_{12}(\varepsilon_{11}\varepsilon_{22} + \varepsilon_{22}\varepsilon_{33} + \varepsilon_{11}\varepsilon_{33}) \\ & + 2c_{44}(\varepsilon_{12}^2 + \varepsilon_{23}^2 + \varepsilon_{13}^2) \Big\} \, \mathrm{d}V, \end{aligned} \tag{19}$$

$$\begin{aligned} E_{\text{elastic2}} = \int \Big\{ & \left[2c_{44}\left(\frac{3}{2}\lambda_{111}\right)^2 - (c_{11} - c_{12})\left(\frac{3}{2}\lambda_{100}\right)^2 \right] \\ & \times (m_1^2 m_2^2 + m_2^2 m_3^2 + m_1^2 m_3^2) \Big\} \, \mathrm{d}V, \end{aligned} \tag{20}$$

$$\begin{aligned} E_{\text{elastic3}} = \int \Big\{ & -\frac{3}{2}\lambda_{100}(c_{11} - c_{12})(\varepsilon_{11} m_1^2 + \varepsilon_{22} m_2^2 + \varepsilon_{33} m_3^2) \\ & - 6\lambda_{111} c_{44}(\varepsilon_{12} m_1 m_2 + \varepsilon_{23} m_2 m_3 + \varepsilon_{13} m_1 m_3) \Big\} \, \mathrm{d}V. \end{aligned} \tag{21}$$

Following Khachaturyan's theory [31], the total strain $\varepsilon_{ij}(\mathbf{r})$ may be represented as the sum of homogeneous and heterogeneous strains:

$$\varepsilon_{ij}(\mathbf{r}) = \bar{\varepsilon}_{ij} + \eta_{ij}(\mathbf{r}). \tag{22}$$

The homogeneous strain is defined in such a way so that

$$\int \eta_{ij}(\mathbf{r}) \, \mathrm{d}V = 0. \tag{23}$$

The homogeneous strain represents the macroscopic shape change of a system generated due to the formation of a domain structure. The heterogeneous strain does not affect the macroscopic shape of a system.

The equilibrium heterogeneous strain satisfies the mechanical equilibrium condition given by the Euler equation with respect to the elastic displacement

$$\sigma_{ij,j} = 0, \tag{24}$$

where σ_{ij} are the stress components and are given by $\sigma_{ij} = c_{ijkl} e_{kl} = c_{ijkl}(\varepsilon_{kl} - \varepsilon_{kl}^0)$.

For the case of homogeneous modulus approximation, the equilibrium heterogeneous strain can be calculated by solving the equation Eq. (24) in Fourier space. First, we introduce a set of displacements $u_i(\mathbf{r})$,

$$\eta_{ij} = \tfrac{1}{2}(u_{i,j} + u_{j,i}). \tag{25}$$

The equations of equilibrium (24) are thus rewritten as

$$c_{ijkl} u_{k,lj} = c_{ijkl} \varepsilon_{kl,j}^0. \tag{26}$$

The general solution of the displacement field for Eq. (26) is given in Fourier space by

$$u_i(\xi) = X_j N_{ij}(\xi)/D(\xi), \tag{27}$$

where $X_i = -ic_{ijkl}\varepsilon_{kl}^0(\xi)\xi_j$, $u_i(\xi)$ and $\varepsilon_{kl}^0(\xi)$ are the Fourier transforms of u_i and ε_{kl}^0, respectively, $N_{ij}(\xi)$ are cofactors of a 3×3 matrix $\mathbf{K}[\xi]$,

$$\mathbf{K}[\xi] = \begin{bmatrix} K_{11} & K_{12} & K_{13} \\ K_{21} & K_{22} & K_{23} \\ K_{31} & K_{32} & K_{33} \end{bmatrix} \tag{28}$$

and $D(\xi)$ is the determinant of matrix $\mathbf{K}[\xi]$. Note that $K_{ki} = c_{kjil}\xi_j\xi_l$.

For cubic crystals, the explicit expressions of $D(\xi)$ and $N_{ij}(\xi)$ are:

$$\begin{aligned} D(\xi) &= \mu^2(\lambda + 2\mu + \chi)\xi^6 \\ &\quad + \mu\chi(2\lambda + 2\mu + \chi)\xi^2(\xi_1^2\xi_2^2 + \xi_1^2\xi_3^2 + \xi_2^2\xi_3^2) \\ &\quad + \chi^2(3\lambda + 3\mu + \chi)\xi_1^2\xi_2^2\xi_3^2, \\ N_{11}(\xi) &= \mu^2\xi^4 + \mu(\lambda + \mu + \chi)\xi^2(\xi_2^2 + \xi_3^2) \\ &\quad + \chi(2\lambda + 2\mu + \chi)\xi_2^2\xi_3^2, \\ N_{12}(\xi) &= -(\lambda + \mu)\xi_1\xi_2(\mu\xi^2 + \chi\xi_3^2) \end{aligned} \tag{29}$$

and other components are obtained by the cyclical permutation of 1, 2, 3, where

$$\lambda = c_{12}, \quad \mu = c_{44}, \quad \chi = c_{11} - c_{12} - 2c_{44}, \quad \text{and} \quad \xi^2 = \xi_i\xi_i. \tag{30}$$

The displacement field $u_i(\mathbf{r})$ in the real space can be obtained through an inverse Fourier transform of $u_i(\xi)$. Consequently, the heterogeneous strain can be calculated by Eq. (25).

The value of the homogeneous strain depends on the boundary conditions. For a clamped boundary condition, the system as a whole is not allowed to deform. Therefore, the homogeneous strain is zero. When a system is subject to a constant homogeneous applied strain $\varepsilon_{ij}^{\text{a}}$, the homogeneous strain is simply equal to the applied strain. If there is no external stress applied and the system is unconstrained with respect to the macroscopic deformation, the homogeneous strain is obtained by minimizing the total elastic energy respect to the homogeneous strain. Substituting Eq. (22) into the total elastic energy given in Eq. (16) and using the fact of Eq. (23), we obtain

$$\begin{aligned} E_{\text{elastic}} &= \int \frac{1}{2} c_{ijkl}\left[\bar{\varepsilon}_{ij} + \eta_{ij}(\mathbf{r}) - \varepsilon_{ij}^0\right]\left[\bar{\varepsilon}_{kl} + \eta_{kl}(\mathbf{r}) - \varepsilon_{kl}^0\right] \mathrm{d}V \\ &= \frac{V}{2} c_{ijkl}\bar{\varepsilon}_{ij}\bar{\varepsilon}_{kl} - c_{ijkl}\bar{\varepsilon}_{ij}\int \varepsilon_{kl}^0 \, \mathrm{d}V + c_{ijkl}\bar{\varepsilon}_{ij}\int \eta_{kl}(\mathbf{r}) \, \mathrm{d}V \\ &\quad + \int \frac{1}{2} c_{ijkl}\left[\eta_{ij}(\mathbf{r}) - \varepsilon_{ij}^0\right]\left[\eta_{kl}(\mathbf{r}) - \varepsilon_{kl}^0\right] \mathrm{d}V \\ &= \frac{V}{2} c_{ijkl}\bar{\varepsilon}_{ij}\bar{\varepsilon}_{kl} - c_{ijkl}\bar{\varepsilon}_{ij}\int \varepsilon_{kl}^0 \, \mathrm{d}V \\ &\quad + \int \frac{1}{2} c_{ijkl}\left[\eta_{ij}(\mathbf{r}) - \varepsilon_{ij}^0\right]\left[\eta_{kl}(\mathbf{r}) - \varepsilon_{kl}^0\right] \mathrm{d}V, \end{aligned} \tag{31}$$

where V is the total volume of the system.

Minimizing it with respect to the homogeneous strain, i.e.,

$$\frac{\partial E_{\text{elastic}}}{\partial \bar{\varepsilon}_{ij}} = 0 = \mathrm{V} c_{ijkl}\bar{\varepsilon}_{kl} - c_{ijkl}\int \varepsilon^0_{kl}\,\mathrm{d}V, \tag{32}$$

we have

$$\bar{\varepsilon}_{kl} = \frac{1}{V}\int \varepsilon^0_{kl}\,\mathrm{d}V. \tag{33}$$

Using the stress-free strain given in Eq. (14), the homogeneous strain is given by:

$$\begin{aligned}
\bar{\varepsilon}_{11} &= \frac{3}{2}\lambda_{100}\left(\overline{m_1^2} - \frac{1}{3}\right), \quad \bar{\varepsilon}_{12} = \frac{3}{2}\lambda_{111}\overline{m_1 m_2},\\
\bar{\varepsilon}_{22} &= \frac{3}{2}\lambda_{100}\left(\overline{m_2^2} - \frac{1}{3}\right), \quad \bar{\varepsilon}_{13} = \frac{3}{2}\lambda_{111}\overline{m_1 m_3},\\
\bar{\varepsilon}_{33} &= \frac{3}{2}\lambda_{100}\left(\overline{m_3^2} - \frac{1}{3}\right), \quad \bar{\varepsilon}_{23} = \frac{3}{2}\lambda_{111}\overline{m_2 m_3},
\end{aligned} \tag{34}$$

where $\overline{m_i^2}$ and $\overline{m_i m_j}$ represent the volume average of m_i^2 and $m_i m_j$ over a system containing a domain structure, respectively.

When a system is subject to a homogeneous applied stress σ^{a}_{ij}, the total potential energy is given by the sum of elastic energy of the system and the potential of the mechanical loading,

$$E_p = E_{\text{elastic}} - V\sigma^{\mathrm{a}}_{ij}\bar{\varepsilon}_{ij}. \tag{35}$$

Minimizing the total potential energy with respect to the homogeneous strain, we have

$$\begin{aligned}
\frac{\partial E_p}{\partial \bar{\varepsilon}_{ij}} &= \frac{\partial E_{\text{elastic}}}{\partial \bar{\varepsilon}_{ij}} - \frac{V\sigma^{\mathrm{a}}_{ij}\bar{\varepsilon}_{ij}}{\partial \bar{\varepsilon}_{ij}}\\
&= \mathrm{V} c_{ijkl}\bar{\varepsilon}_{kl} - c_{ijkl}\int \varepsilon^0_{kl}\,\mathrm{d}V - V\sigma^{\mathrm{a}}_{ij} = 0.
\end{aligned} \tag{36}$$

Therefore

$$\bar{\varepsilon}_{kl} = \frac{1}{V}\int \varepsilon^0_{kl}\,\mathrm{d}V + s_{ijkl}\sigma^{\mathrm{a}}_{ij}, \tag{37}$$

where s_{ijkl} is the elastic compliance tensor. Using Eq. (14), we obtain the homogeneous strain:

$$\begin{aligned}
\bar{\varepsilon}_{11} &= s_{11}\sigma^{\mathrm{a}}_{11} + s_{12}(\sigma^{\mathrm{a}}_{22} + \sigma^{\mathrm{a}}_{33}) + \frac{3}{2}\lambda_{100}\left(\overline{m_1^2} - \frac{1}{3}\right),\\
\bar{\varepsilon}_{12} &= \frac{1}{2}s_{44}\sigma^{\mathrm{a}}_{12} + \frac{3}{2}\lambda_{111}\overline{m_1 m_2},\\
\bar{\varepsilon}_{22} &= s_{11}\sigma^{\mathrm{a}}_{22} + s_{12}\left(\sigma^{\mathrm{a}}_{11} + \sigma^{\mathrm{a}}_{33}\right) + \frac{3}{2}\lambda_{100}\left(\overline{m_2^2} - \frac{1}{3}\right),\\
\bar{\varepsilon}_{13} &= \frac{1}{2}s_{44}\sigma^{\mathrm{a}}_{13} + \frac{3}{2}\lambda_{111}\overline{m_1 m_3},\\
\bar{\varepsilon}_{33} &= s_{11}\sigma^{\mathrm{a}}_{33} + s_{12}(\sigma^{\mathrm{a}}_{11} + \sigma^{\mathrm{a}}_{22}) + \frac{3}{2}\lambda_{100}\left(\overline{m_3^2} - \frac{1}{3}\right),\\
\bar{\varepsilon}_{23} &= \frac{1}{2}s_{44}\sigma^{\mathrm{a}}_{23} + \frac{3}{2}\lambda_{111}\overline{m_2 m_3},
\end{aligned} \tag{38}$$

where s_{11}, s_{12}, and s_{44} are the three independent compliance constants for a cubic material in the Voigt's notion.

The total strain can be calculated by Eq. (22). Consequently, the elastic energy can be obtained for a magnetostrictive material with an arbitrary magnetic domain structure by Eq. (16).

3. Simulation results and discussion

The magnetic domain structures are obtained by the numerically solving the LLG equation using the Gauss–Seidel projection method in this work [39]. The LLG equation can be rewritten in dimensionless form, by employing the following set of dimensionless variables:

$$\begin{aligned}
&\mathbf{M} = M_{\mathrm{s}}\mathbf{m},\\
&\mathbf{H}_{\text{eff}} = M_{\mathrm{s}}\mathbf{h}_{\text{eff}},\\
&t = \frac{1+\alpha^2}{\gamma_0 M_{\mathrm{s}}}\tau.
\end{aligned} \tag{39}$$

The equation becomes,

$$\frac{\partial \mathbf{m}}{\partial \tau} = -\mathbf{m}\times\mathbf{h}_{\text{eff}} - \alpha\mathbf{m}\times(\mathbf{m}\times\mathbf{h}_{\text{eff}}). \tag{40}$$

We can rewrite the effective magnetic field as

$$\begin{aligned}
\mathbf{h}_{\text{eff}} &= \frac{1}{M_{\mathrm{s}}}(\mathbf{H}_{\text{eff}1} + \mathbf{H}_{\text{eff}2})\\
&= \frac{1}{M_{\mathrm{s}}}\left[\left(-\frac{1}{\mu_0}\frac{\partial E_{\text{exch}}}{\partial \mathbf{M}}\right) + \left(-\frac{1}{\mu_0}\frac{\partial E'}{\partial \mathbf{M}}\right)\right]\\
&= A^*\Delta\mathbf{m} + \frac{1}{M_{\mathrm{s}}}\left(-\frac{1}{\mu_0}\frac{\partial E'}{\partial \mathbf{M}}\right)\\
&= A^*\Delta\mathbf{m} + \mathbf{h}[\mathbf{m}],
\end{aligned} \tag{41}$$

where E' is the total free energy excluding the exchange energy part. A^* is defined as $A^* = 2A/\mu_0 M_{\mathrm{s}}^2 l_{\mathrm{d}}^2$, where l_{d} is the cell size in the model.

Following Ref. [39], we solve the equation

$$\frac{\partial \mathbf{m}}{\partial \tau} = -\mathbf{m}\times(A^*\Delta\mathbf{m} + \mathbf{h}[\mathbf{m}]) - \alpha\mathbf{m}\times(\mathbf{m}\times(A^*\Delta\mathbf{m} + \mathbf{h}[\mathbf{m}])) \tag{42}$$

in three steps:

Step 1:

$$\begin{aligned}
g_i^n &= (1 - A^*\Delta\tau\Delta)^{-1}(m_i^n + \Delta\tau h_i[\mathbf{m}^n]),\\
g_i^* &= (1 - A^*\Delta\tau\Delta)^{-1}(m_i^* + \Delta\tau h_i[\mathbf{m}^n]), \quad i = 1,2,3.
\end{aligned} \tag{43}$$

$$\begin{pmatrix} m_1^* \\ m_2^* \\ m_3^* \end{pmatrix} = \begin{pmatrix} m_1^n + (g_2^n m_3^n - g_3^n m_2^n) \\ m_2^n + (g_3^n m_1^* - g_1^* m_3^n) \\ m_3^n + (g_1^* m_2^* - g_2^* m_2^*) \end{pmatrix}. \tag{44}$$

Step 2:

$$\begin{pmatrix} m_1^{**} \\ m_2^{**} \\ m_3^{**} \end{pmatrix} = \begin{pmatrix} m_1^{*} + \alpha\Delta\tau(A^*\Delta m_1^{**} + h_1[\mathbf{m}^*]) \\ m_2^{*} + \alpha\Delta\tau(A^*\Delta m_2^{**} + h_2[\mathbf{m}^*]) \\ m_3^{*} + \alpha\Delta\tau(A^*\Delta m_3^{**} + h_3[\mathbf{m}^*]) \end{pmatrix}. \quad (45)$$

Step 3:

$$\begin{pmatrix} m_1^{n+1} \\ m_2^{n+1} \\ m_3^{n+1} \end{pmatrix} = \frac{1}{|m^{**}|}\begin{pmatrix} m_1^{**} \\ m_2^{**} \\ m_3^{**} \end{pmatrix}. \quad (46)$$

We solve Eqs. (43) and (45) by employing the Fourier transform. For example, by Fourier transforming both sides of Eq. (43), the equation becomes

$$g_i^n(\xi) = \frac{m_i^n(\xi) + \Delta\tau\tilde{h}_i[\mathbf{m}^n]}{1 + (\xi_1^2 + \xi_3^2 + \xi_3^2)A^*\Delta\tau}, \quad (47)$$

where $g_i^n(\xi), m_i^n(\xi)$, and $\tilde{h}_i[\mathbf{m}^n]$ are the Fourier transforms of g_i^n, m_i^n, and $h_i[\mathbf{m}^n]$, respectively. The value of g_i^n in real space can be obtained by doing an inverse Fourier transform of $g_i^n(\xi)$. Eq. (45) can be solved in a similar way.

3.1. Domain structures and magnetostriction in FeGa

We first consider $Fe_{81.3}Ga_{18.7}$ as an example for the numerical simulations. The corresponding material parameters are from Refs. [3–5]: $M_s = 1.432\times10^6$ A/m, $K_1 = 2\times10^4$ J/m^3, $K_2 = -4.5\times10^4$ J/m^3, and $\lambda_{100} = 2.64\times10^{-4}$, $\lambda_{111} = 0$. The bulk cubic elastic constants are $c_{11} = 1.96\times10^{11}$ N/m^2, $c_{12} = 1.56\times10^{11}$ N/m^2, and $c_{44} = 1.23\times10^{11}$ N/m^2. To save the computational time and since the magnetic easy axes are along $\langle 1\,0\,0\rangle$ directions, we performed the simulations with ($512\times 512\times 1$ or $256\times256\times1$) discrete cells, i.e., essentially 2D systems. Periodic boundary conditions are applied along the x_1, x_2 and x_3 axes. The magnetization is assumed to be uniform in each cell, but it is allowed to rotate in three dimensions (3D). For the damping constant, a value of $\alpha = 0.5$ is used in the simulation. In reduced variables, the exchange stiffness constant is chose be $A^* = 0.0625$, and the time step is $\Delta\tau = 0.1$.

3.1.1. Energetic contributions and domain structures

Giant magnetostrictive materials usually exhibit rather complicated domain structures resulted from competing energetic contributions such as elastic energy and magnetostatic energy. To understand the relation of each energetic contribution to the resulting domain structure, we performed simulations taking into account different energy contributions.

The domain structures obtained are shown in Figs. 1, 3–5. Fig. 1 shows the temporal evolution of a domain structure in the presence of elastic energy but without the magnetostatic energy. Mechanical clamped boundary conditions were used, which means that the overall dimensions of the system do not change. At the beginning, the random initial configuration evolves to domains as shown in Fig. 1(a). All the six different kinds of orientation domains determined by the cubic anisotropy energy, including the domains with magnetization along the positive x_1 direction ([1 0 0] domain), negative x_1 direction ([$\bar{1}$ 0 0] domain), positive x_2 direction ([0 1 0] domain), negative x_2 direction ([0 $\bar{1}$ 0] domain), positive x_3 direction ([0 0 1] domain), and negative x_3 direction ([0 0 $\bar{1}$] domain), are present with almost equal fractions. Fig. 1(b) illustrates the domain structure after 40,000 steps of evolution, indicating domain growth and coarsening. The domains are separated by 180° or 90° domain walls. A schematic diagram showing the 180° domain and 90° domain walls separating the domains is given in Fig. 2. The 90° domain walls tend to align along the [1 1 0] or [1 $\bar{1}$ 0] directions separating [1 0 0] domain (or [$\bar{1}$ 0 0] domain) and [0 1 0] domain (or [0 $\bar{1}$ 0] domain). The alignment becomes increasingly strong at the later stage of evolution as shown in Fig. 1(c) and (d). Since in this case, the magnetostatic energy is not included and the exchange energy is isotropic, the domain wall alignment must be entirely due to the anisotropic elastic interactions. For 90° domain walls, the condition of elastic compatibility between the associated domain pairs requires that the tangential components of the

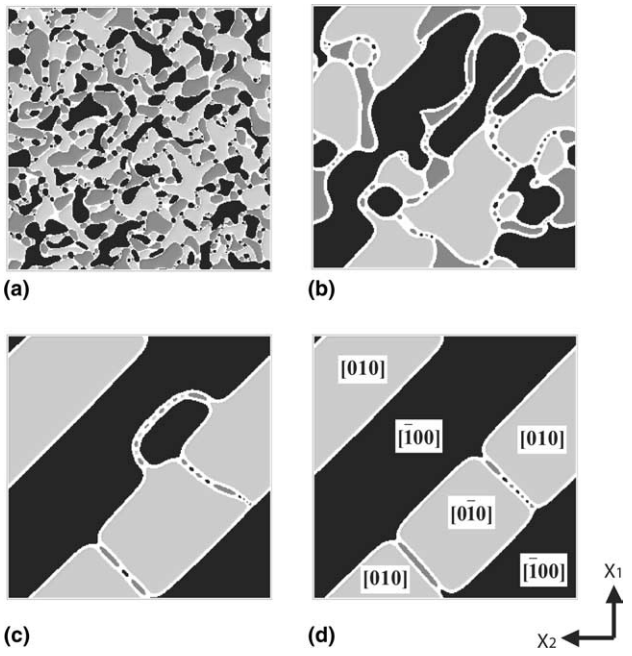

Fig. 1. Domain evolution in the presence of elastic energy but the absence of magnetostatic energy: (a) 4000 steps; (b) 40,000 steps; (c) 200,000 steps; (d) 400,000 steps. Black = [1 0 0] and [$\bar{1}$ 0 0] domains, light gray = [0 1 0] and [0 $\bar{1}$ 0] domains, and dark gray = [0 0 1] and [0 0 $\bar{1}$] domains.

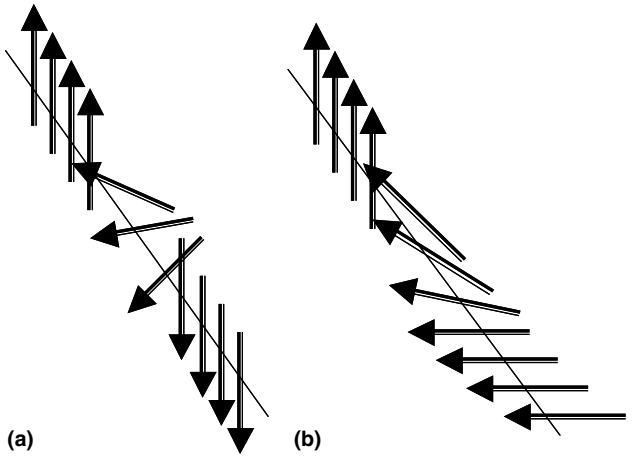

Fig. 2. Schematic diagram of the 180° domain wall and 90° domain wall separating the domains: (a) 180° domain wall; (b) 90° domain wall.

stress-free strain must be equal in both domains for the given wall orientation. For a pair of [1 0 0] (or $[\bar{1}\,0\,0]$) and [0 1 0] (or $[0\,\bar{1}\,0]$) domains, the corresponding wall plane is (1 1 0) (or $(1\,\bar{1}\,0)$), which is automatically predicted by the simulations without a priori assumptions. For 180° domain walls, since the magnetizations are anti-parallel on either side of the wall and correspond to identical strains, there is no preferred orientation of the 180° domain walls as shown in Fig. 1(b) and (c). It is interesting to note that the 180° domain walls become straight and perpendicular to the neighboring 90° domain walls as shown in Fig. 1(d). The directional alignment for the 180° walls can be easily understood as a result of domain wall minimization associated with the straight domain walls. Periodic segments were observed in some 180° domain walls as shown in Fig. (1). Similar substructures along 180° domain walls have been observed and studied experimentally [40], in which case the subdivision of domain wall was explained as a result of magnetostatic energy minimization. To reveal the origin of the subdivision of the 180° domain wall observed here, we simulated the domain structure without considering both the magnetostatic energy and elastic energy. As Fig. (3) shows, the substructures along 180° domain walls still exist, which indicates that neither the magnetostatic energy nor elastic energy is responsible for the formation of the substructure. They are formed due to degeneracy of the domain wall with four different orientations that have equal energy. It is also noted, as expected, that since the magnetostatic energy is absent, both the head to tail and head to head (tail to tail) domain walls exist in the domain structure.

One may also notice that in Fig. 1 the fraction of [0 0 1] domain and $[0\,0\,\bar{1}]$ domain decreases with time. Eventually as shown in Fig. 1(c) and (d), only those [1 0 0] (or $[\bar{1}\,0\,0]$) and [0 1 0] (or $[0\,\bar{1}\,0]$) domains survive. This is easily understandable since this is a quasi 2D

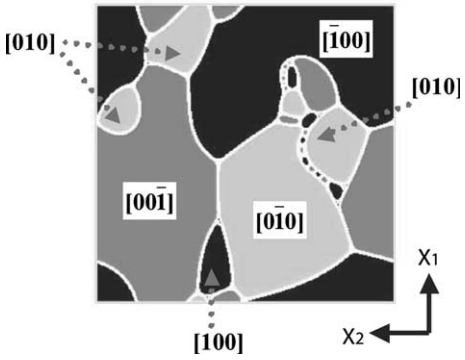

Fig. 3. Simulated domain structure in the absence of both magnetostatic and elastic energies. Black = [1 0 0] and $[\bar{1}\,0\,0]$ domains, light gray = [0 1 0] and $[0\,\bar{1}\,0]$ domains, and dark gray = [0 0 1] and $[0\,0\,\bar{1}]$ domains.

simulation, and hence the domain walls between [0 0 1] (or $[0\,0\,\bar{1}]$) domains and the other four domains with magnetization perpendicular to the x_3 axis are parallel to the [0 0 1] direction instead of the energetically favorable $(0\,1\,1)/(0\,1\,\bar{1})$ or $(1\,0\,1)/(\bar{1}\,0\,1)$ planes.

Experimental results [3–5] showed that the magnetostrictive constant of FeGa alloy is sensitive to the material composition and temperature. Therefore, it is useful to study the domain structure of magnetostrictive materials with different magnetostriction constants. Fig. 4 shows the simulated domain structure with varying magnetostrictive constants: $\lambda_{100} = 1.32 \times 10^{-4}$, 2.64×10^{-5} ($\lambda_{111} = 0$), which are 0.5 and 0.1 times of that for $Fe_{81.3}Ga_{18.7}$, respectively. With the decrease of magnetostrictive constant, the domain walls become less aligned, since the contribution of elastic energy becomes increasingly insignificant. We also note that the $[0\,0\,\bar{1}]$ domains survive for the case of low magnetostrictive constants, which confirm the responsibility of the elastic energy for the disappearance of [0 0 1] (or $[0\,0\,\bar{1}]$) domains in materials with high magnetostrictive constants in our 2D simulations as shown in Fig. 1.

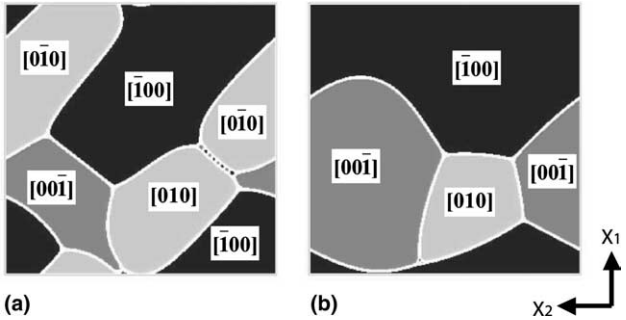

Fig. 4. Simulated domain structure with varying magnetostrictive constants: (a)$\lambda_{100} = 1.32 \times 10^{-4}$, $\lambda_{111} = 0$; (b) $\lambda_{100} = 2.64 \times 10^{-5}$, $\lambda_{111} = 0$ (in the presence of elastic energy but the absence of magnetostatic energy). Black = [1 0 0] and $[\bar{1}\,0\,0]$ domains, light gray = [0 1 0] and $[0\,\bar{1}\,0]$ domains, and dark gray = [0 0 1] and $[0\,0\,\bar{1}]$ domains.

It should be noted that some other material parameters of FeGa alloy beside magnetostriction constants were also found to depend on composition and temperature, such as saturation magnetization and cubic anisotropy constant. They should also affect the domain structure of FeGa alloy, which was not studied in this work. Thus, complicated behaviors of domain structures in FeGa are expected depending on composition and temperature.

Fig. 5 shows the temporal evolution of domain structure when the magnetostatic energy and elastic energy are both taken into account. In this case, the domain wall orientation is constrained by both the elastic compatibility and the magnetic compatibility. Two adjacent domains are magnetically compatible if the normal components of the magnetization vectors of both domains with respect to their common domain wall are equal. Therefore, only head to tail domain walls survive. Since the discontinuities in the strain do not occur for 180° domain walls, the 180° domain walls are only constrained by the magnetic compatibility. It is shown that the 180° domain walls are found to be parallel to the magnetization direction of associated domain pair (Fig. 5(d)). Finally, a twin-like domain structure was obtained as

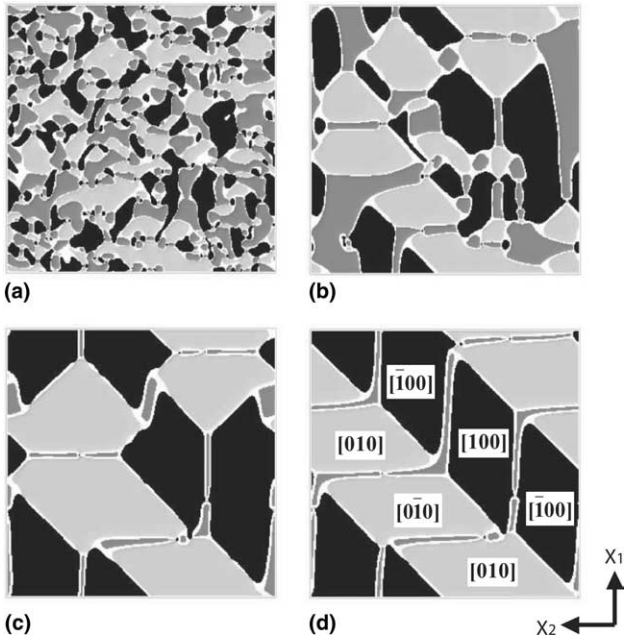

Fig. 5. Domain evolution in the presence of both elastic energy and magnetostatic energy: (a) 4000 steps; (b) 40,000 steps; (c) 200,000 steps; (d) 500,000 steps. Black = [1 0 0] and [$\bar{1}$ 0 0] domains, light gray = [0 1 0] and [0 $\bar{1}$ 0] domains, and dark gray = [0 0 1] and [0 0 $\bar{1}$] domains.

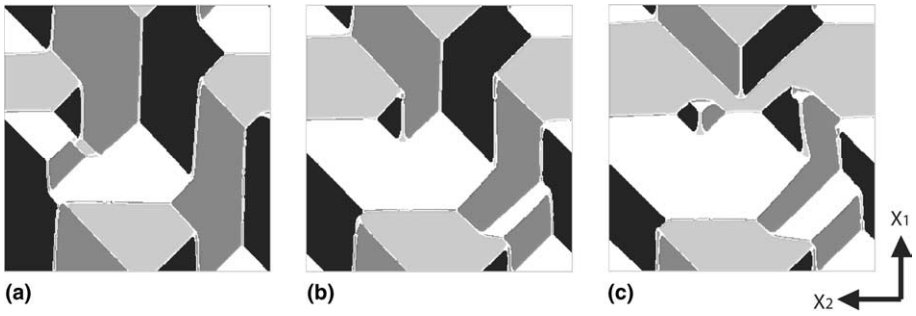

Fig. 6. Simulated domain structure with different applied pre-stress (along x_1 axis): (a) 5 MPa (61% domain with magnetization along x_1 axis); (b) 0 MPa (49%); (c) −5 MPa (32%). Dark gray = [1 0 0] domains, black = [$\bar{1}$ 0 0] domains, light gray = [0 $\bar{1}$ 0] domains, and white = [0 1 0] domains.

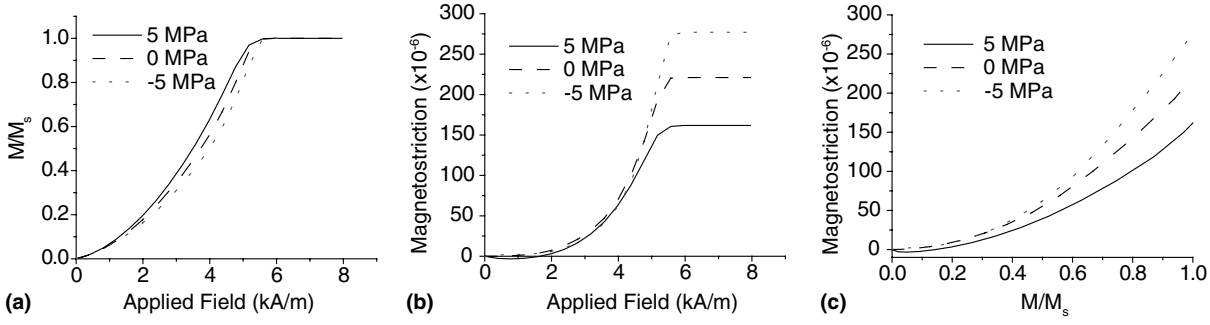

Fig. 7. The field dependence of magnetization and magnetostriction for the giant magnetostrictive material with different pre-stress applied: (a) M/M_s vs. applied field curves; (b) magnetostriction vs. applied field curves; (c) magnetostriction vs. M/M_s curves.

shown in Fig. 5(d), which is similar to that described in a prior theoretical prediction [17]. If the exchange stiffness constant of $Fe_{81.3}Ga_{18.7}$ has a similar magnitude as Fe ($A \sim 10^{-11}$ J/m), the system studied here is around 3×3 μm.

3.1.2. Magnetization process

The overall strain response of a magnetostrictive material is directly related to the domain evolution in the material under applied fields. The field-induced magnetostriction under a certain applied field depends on the initial demagnetized domain structure in a crystal. The largest magnetostriction appears only when an ideal initial domain structure is formed, i.e., all the domains align perpendicular to the applied magnetic field direction. Such an alignment can be obtained by an applied pre-stress. From Eq. (21), it can easily been seen that the elastic energy contribution can alter the anisotropy energy. For the positive λ_{100} we used here, a tensile stress, that produces an elongation in the x_1 axis (and hence contraction in x_2 and x_3 axes), energetically favors the domains with magnetization along the x_1 axis while

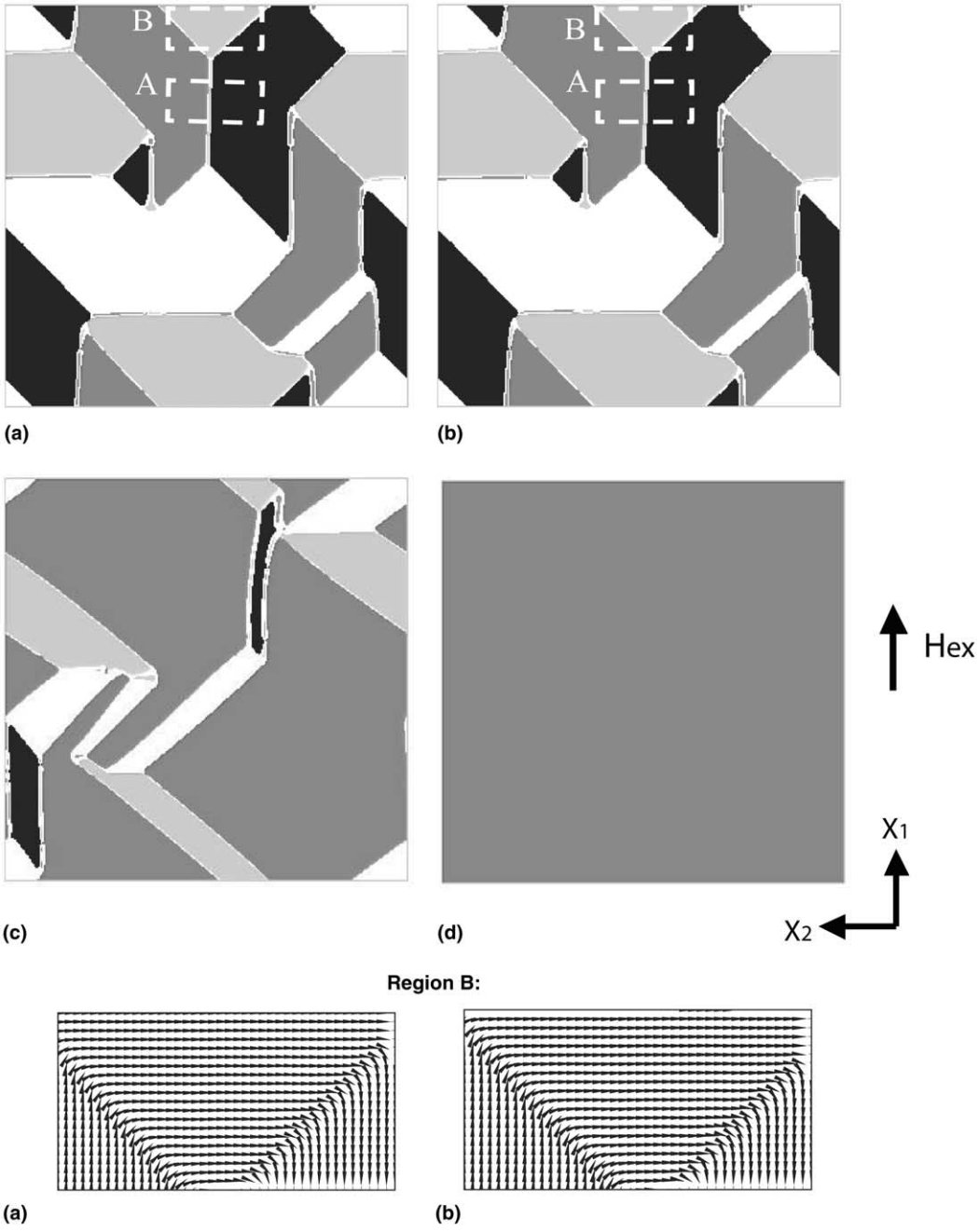

Fig. 8. The domain structure evolution under applied field along [1 0 0] (without pre-stress): (a) 0 kA/m; (b) 0.80 kA/m; (c) 4.38 kA/m; (d) 7.96 kA/m. Dark gray = [1 0 0] domains, black = $[\bar{1}\,0\,0]$ domains, light gray = $[0\,\bar{1}\,0]$ domains, and white = [0 1 0] domains.

a compressive stress will favor domains with magnetization perpendicular to the x_1 axis. Fig. 6 shows the domain structures of samples with different applied pre-stresses. As expected, while a tensile stress increases the fraction of domains along x_1 axis, a compressive stress applied along x_1 axis decreases it.

The magnetostriction and associated domain structure evolution under an applied magnetic field for the samples with different applied pre-stress were shown in Figs. 7 and 8. In prior experiments [3–5], to obtain large magnetostriction at a relatively low magnetic field, the samples were usually prepared in the shapes of a thin disk or a rod to decrease the demagnetization effect. To approximate this case, in our simulation we use the demagnetizing factor of infinite thin sheet ($N_x = N_y = 0, N_z = 1$). A magnetostriction vs. M/M_s curve for the magnetization process was given in Fig. 7(c). The initial flat stage of the curve show that the initial increase of magnetization is accompanied by a small magnetostrictive change. As Fig. (8) shows, such an initial magnetization stage mainly consist of 180° domain wall movement (such as region A in Fig. 8(a) and (b)), which does not produce any magnetostrictive change in dimensions. 90° domain wall movement also occurred by switching from $[\bar{1}00]$ to $[010]$ (or $[0\bar{1}0]$) domains or from $[010]$ (or $[0\bar{1}0]$) to $[100]$ domains (such as region B in Fig. 8(a) and (b)). As magnetostriction vs. M/M_s curve measures the average behavior of the system, the effect of such two distinct 90° domain wall motion is equal to a 180° domain switching from $[\bar{1}00]$ to $[100]$ domain, which does not produce magnetostrictive change. With further magnetization, the fraction of the $[\bar{1}00]$ domain deceases, and the associated 180° domain switching decreases too. As shown in the magnetostriction vs. M/M_s curve, the slope increases with magnetization. Finally, a single domain with saturated magnetization and magnetostriction along the applied field was obtained as shown in Fig. 8(d). It is shown that a pre-stress can indeed have a significant effect on the magnetostriction. A larger saturation magnetostriction was obtained for systems with a compressive pre-stress, while a smaller magnetostriction was obtained when a tensile pre-stress was applied.

3.2. 3D Domain structures in Terfenol-D

As Terfenol-D has a negative magnetocrystalline anisotropy with easy directions along $\langle 111 \rangle$, it is not possible to approximate the domain structures in 2D. Therefore, we chose a 3D system with $128 \times 128 \times 128$ cells. The periodic boundary conditions are applied along all three Cartesian axes. The material parameters are [26]: $M_s = 8.0 \times 10^5$ A/m, $A = 9 \times 10^{-12}$ J/m, $K_1 = -6 \times 10^4$ J/m^3, $K_2 = 0$ J/m^3 and $\lambda_{100} = 0$, $\lambda_{111} = 1.64 \times 10^{-3}$. The bulk cubic elastic constants are $c_{11} = 1.41 \times 10^{11}$ N/m^2, $c_{12} = 6.48 \times 10^{10}$ N/m^2, and $c_{44} = 4.87 \times 10^{10}$ N/m^2. Because of the extensive computational time required for 3D simulations, in this paper we only focused on the prediction of 3D domain structures without an applied field. An example of 3D domain structure is shown in Fig. 9. Domains with magnetization along the 8 possible $\langle 111 \rangle$ easy directions were observed. The obtained domain wall orientations of non-180° walls, which constrained by the elastic compatibility, agree with those predicted by theory of James and Kinderlehrer [17,18] and with prior experimental observations [6,11]. It should be emphasized that these domain wall orientations were predicted without a priori assumptions. The orientations of 180° domain wall are not exactly along those planes determined by the magnetic compatibility, which comes from the competition between magnetostatic and exchange energy, since the exchange energy prefers a flat domain wall with minimization of wall. Extensive studies on the magnetic behavior of Terfenol-D such as the magnetic process with applied magnetic field or stress will be carried out using extensive 3D simulations.

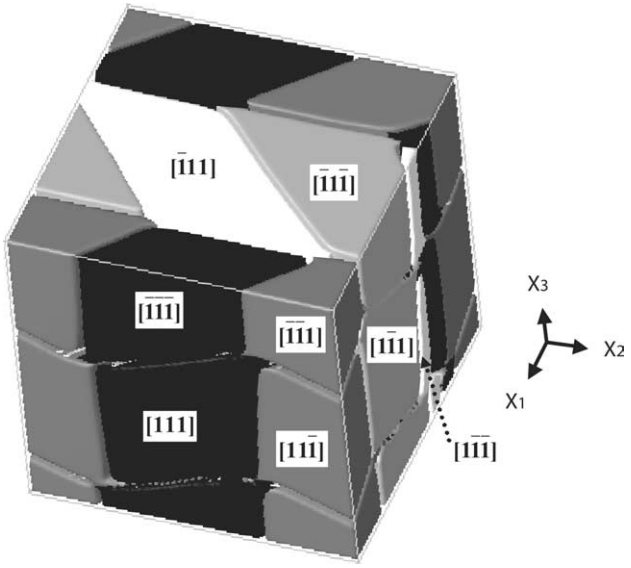

Fig. 9. Simulated domain structure of Terfenol-D. Black = [1 1 1] and $[\bar{1}\,\bar{1}\,\bar{1}]$ domains, dark gray = $[1\,1\,\bar{1}]$ and $[\bar{1}\,\bar{1}\,1]$ domains, light gray = $[1\,\bar{1}\,1]$ and $[\bar{1}\,1\,\bar{1}]$ domains, and white = $[1\,\bar{1}\,\bar{1}]$ and $[\bar{1}\,1\,1]$ domains.

4. Conclusion

A computational model for predicting the stability of domain structures and their temporal evolution in giant magnetostrictive materials is developed by combining a micromagnetic model with the phase-field microelasticity of Khachaturyan for arbitrary domain structures. It takes into account both the inhomogeneous stress and magnetic field distributions in a domain structure. Its applications to FeGa and Terfenol-D demonstrated that the model correctly predicts the domain wall orien-

tations as well as the domain structure evolution and the magnitude of magnetostriction during a magnetization process. It is shown that the elastic energy minimization results in an alignment of 90° domain wall orientation while the magnetostatic energy is responsible for the orientation of 180° domain walls and the head–tail magnetization configuration across a domain wall. Subdivision of 180° domain walls was observed, which was attributed to the degeneracy of the domains with different magnetic easy directions rather than the elastic interactions or the magnetostatic interactions that were believed to be responsible previously. Under an applied magnetic field, the domain structure evolution starts with the 180° domain switching, which does not produce any magnetostriction. It is also demonstrated that prestress can be efficiently used to increase the magnetostriction changing the initial magnetic domain structure in the demagnetization state.

Acknowledgment

The authors are grateful for the financial support by the National Science Foundation under the Grant No. DMR 01-22638.

References

[1] Clark AE. Magnetostrictive rare earth-Fe_2 compounds. In: Wohlfarth EP, editor. Ferromagnetic materials. Amsterdam: North-Holland; 1980.
[2] Jiles DC. J Phys D: Appl Phys 1994;27:1.
[3] Clark AE, Restorff JB, Wun-Fogle M, Lograsso TA, Schlagel DL. IEEE Trans Mag 2000;36:3238.
[4] Clark AE, Hathaway KB, Wun-Fogle M, Restorff JB, Lograsso TA, Keppens VM, et al. J Appl Phys 2003;93:8621.
[5] Rafique S, Cullen JR, Wuttig M, Cui J. J Appl Phys 2004;95:6939.
[6] Engdahl G. Handbook of giant magnetostrictive material. New York, NY: Academic Press; 2000.
[7] Holden AP, Lord DG, Grundy PJ. J Appl Phys 1996;79:4650.
[8] Dooley J, Graef MD, McHenry ME. J Appl Phys 1998;83:6837.
[9] Holden AP, Lord DG, Grundy PJ. J Appl Phys 1996;79:6070.
[10] Lord DG, Holden AP, Grundy PJ. J Appl Phys 1997;81:5728.
[11] Schmidt J, Tickle R, Skidmore GD, Merton C, James RD, Dahlberg ED. J Magn Magn Mater 1998;190:98.
[12] Shull RD, Quandt E, Shapiro AT, Glasmachers S, Wuttig M. J Appl Phys 2004;95:6948.
[13] Busbridge SC, Piercy AR. J Appl Phys 1993;73:5354.
[14] Wang BW, Busbridge SC, Li YX, Wu GH, Piercy AR. J Magn Magn Mater 2000;218:198.
[15] Wang BW, Busbridge SC, Guo ZJ, Zhang ZD. J Appl Phys 2003;93:8489.
[16] Brown WF. Magnetoelastic interactions. Berlin: Springer; 1966.
[17] James RD, Kinderlehrer D. Philos Mag B 1993;68:237.
[18] James RD, Kinderlehrer D. J Appl Phys 1994;76:7012.
[19] DeSimone A, James RD. J Mech Phys Solids 2002;50:283.
[20] Jiles DC, Thoelke JB. J Magn Magn Mater 1994;134:143.
[21] DeSimone A, James RD. J Appl Phys 1997;81:5706.
[22] Zhao XG, Lord DG. J Magn Magn Mater 1999;195:699.
[23] Armstrong WD. J Appl Phys 2002;91:2202.
[24] Park WJ, Son DR, Lee ZH. J Magn Magn Mater 2002;248:223.
[25] Zhu B, Lo CCH, Lee SJ, Jiles DC. J Appl Phys 2001;89:7009.
[26] Shu YC, Lin MP, Wu KC. Mech Mater 2004;36:975.
[27] Fabian K, Heider F. Geophys Res Lett 1996;23:2839.
[28] Shu YC, Yen JH. Mater Res Soc Symp Proc 2004;785:D13.4.1.
[29] Hubert A, Schafer R. Magnetic domains: the analysis of magnetic microstructure. Berlin: Springer; 1998.
[30] Khachaturyan AG, Shatalov GA. Sov Phys JETP 1969;29:557.
[31] Khachaturyan AG. Theory of structural transfomations in solid. New York, NY: Wiley; 1983.
[32] Chen LQ, Wang YZ, Khachaturyan AG. Philos Mag Lett 1992;65:15.
[33] Wang Y, Khachaturyan AG. Acta Mater 1997;45:759.
[34] Jin YM, Artemev A, Khachaturyan AG. Acta Mater 2001;49:2309.
[35] Chen LQ, Hu SY. Phase-field method applied to strain-dominated microstructure evolution during solid-state phase transformations. In: Raabe D, Barlat F, Roters F, Chen LQ, editors. Continuum scale simulation of engineering materials – fundamentals – microstructures – process applications. New York, NY: John Wiley; 2004.
[36] Li YL, Hu SY, Liu ZK, Chen LQ. Appl Phys Lett 2001;78:3878.
[37] Li YL, Hu SY, Liu ZK, Chen LQ. Acta Mater 2002;50:395.
[38] Seol DJ, Hu SY, Li YL, Shen J, Oh KH, Chen LQ. Acta Mater 2003;51:5173.
[39] Wang XP, Garcia-Cervera CJ, E WN. J Comput Phys 2001;171:357.
[40] Hartmann U, Mende HH. J Appl Phys 1986;59:4123.